International Journal of Cast Metals Research

ISSN: 1364-0461 (Print) 1743-1336 (Online) Journal homepage: http://www.tandfonline.com/loi/ycmr20

Distribution of Al in Al–Si Alloys during electromagnetic continuous casting with cylindrical open ended crucible

X. Bai, J. Li, Z. Fu, Y. Li, B. Ban, T. Zhang, Z. Peng, C. Wang & J. Chen

To cite this article: X. Bai, J. Li, Z. Fu, Y. Li, B. Ban, T. Zhang, Z. Peng, C. Wang & J. Chen (2015) Distribution of Al in Al–Si Alloys during electromagnetic continuous casting with cylindrical open ended crucible, International Journal of Cast Metals Research, 28:5, 269-275, DOI: 10.1179/1743133615Y.0000000010

To link to this article: https://doi.org/10.1179/1743133615Y.0000000010

RESEARCH PAPER

Distribution of Al in Al–Si Alloys during electromagnetic continuous casting with cylindrical open ended crucible

X. Bai*[1], J. Li[2], Z. Fu[1], Y. Li[2], B. Ban[2], T. Zhang[2], Z. Peng[1], C. Wang[1] and J. Chen[2]

Electromagnetic continuous casting (EMCC) exhibits great potential for silicon purification by Al–Si method. Distribution of Al in Al–Si alloys with different aluminium contents during EMCC was investigated. The macrostructure of the Al–Si alloy ingots reveals that the content of primary silicon plates in hypereutectic alloys decreases from the bottom to the top of the ingots, and no obvious primary silicon plate exists in eutectic alloy. The fitting results of aluminium distribution in the alloys reveal two types of aluminium distribution patterns in hypereutectic Al–Si alloys: Scheil model for high temperature solidification and initial transient model for low temperature one. An apparent segregation coefficient of Al is proposed to characterise the solidification process, which is ~0.83 in the hypereutectic alloys.

Keywords: Aluminium distribution, Al–Si alloy, Electromagnetic continuous casting, Solidification models, Apparent segregation coefficient

Introduction

Al–Si alloys are widely used in aerospace, automobile and electronic industries due to their excellent wear and corrosion resistance, low density, low coefficient of thermal expansion and good strength and castability.[1–4] Recently, hypereutectic Al–Si alloy has been selected for solvent refining of metallurgical grade silicon in industry[5] and further theoretically studied by others.[6–8] For the past few years, directional solidification was combined with the solvent refining in the hypereutectic Al–Si alloy.[9] In addition, the effect of electromagnetic stirring on the removal of impurities in the Al–Si melt was reported by Morita *et al.*[10–12] and Yu.[13] In the current work, electromagnetic continuous casting (EMCC) was applied. This method has the following advantages over normal directional solidification: casting ingots of any length, electromagnetic stirring of melt and no pollution to the ingots.

On the other hand, the Al distribution is important because the properties of Al–Si alloys are determined by the local composition in a very large degree. For example, Nikanorov[14] studied the structure and the mechanical properties of binary aluminium–silicon alloys of different compositions. Peres[15] investigated macrostructural and microstructural development in Al–Si alloys directionally solidified under unsteady state conditions. In addition, for impurities removal, Morita reported that the segregation coefficients of B and P decrease with increase in Al content.[11] All these studies contribute to the understanding of the effect of Al content on the properties and the removal process of impurities in the Al–Si alloys. However, the microstructure of the samples and the results presented in these studies only give a qualitative description on the solute distribution. The content of the primary silicon phases in the hypereutectic alloys decreases from the bottom to the top of the samples. However, the quantitative distribution of Al and the effect of different Al contents on its distribution in the hypereutectic Al–Si alloys during directional solidification were not studied in the literature. Additionally, mathematical models have never been applied to describe the Al distribution in directional solidification. In addition, it was found that there are two different distribution types in the hypereutectic Al–Si alloys during directional solidification in the present work.

In this work, three hypereutectic (60, 70 and 80%Al) and one eutectic (87.4%Al) Al–Si alloys were prepared by EMCC. The mass fractions of Al from the bottom to the top of the ingots were calculated by measuring silicon fraction after removing eutectic aluminium by acid washing. In addition, an apparent segregation coefficient is proposed to characterise the solute distribution in the directional solidification process of the hypereutectic and eutectic alloys. The Scheil model and initial transient model are used to fit the experimental data, which are compared with experimental results.

Experimental

Materials and equipment

Metallurgical grade silicon and commercial aluminium were used as raw materials. The contents of the impurity elements in these materials determined by inductively coupled plasma optical emission spectrometer are listed in Table 1.

Al–Si alloy ingots were melted in a SPZ-25 medium frequency induction furnace under Ar atmosphere. The schematic drawing of the furnace is shown in Fig. 1.

[1]School of Engineering and Technology, China University of Geosciences, Beijing 100083, China
[2]Key Laboratory of Novel Thin Film Solar Cells, Institute of Plasma Physics, Chinese Academy of Science, Hefei, 230031, China

*Corresponding author, email xiaolong_89@163.com

Received 20 August 2014; accepted 25 April 2015
DOI 10.1179/1743133615Y.0000000010

Table 1 Impurity content in raw materials/ppmw

Impurity element	Al	Fe	Ca	B	P	Cu	Mg
In silicon	2434	2818	37	25	43	35	8
In aluminium	Bal.	14 152	111	1	26	28	60
Impurity element	Mn	Sn	V	Zn	Ti	Cr	Ni
In silicon	105	7	351	1	437	7	154
In aluminium	41	4	171	47	33	18	49

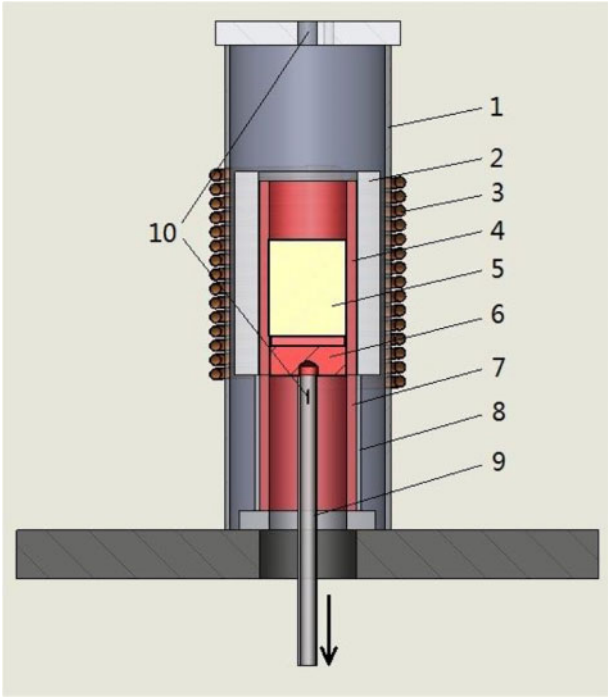

1 Schematic drawing of furnace

Alloys preparation

All the alloys were melted by the same continuous casting process. Typical process is as follows. About 1500 g of raw materials of the nominal composition was put in a graphite heater tube. The graphite tube is 80 mm in inner diameter, 100 mm in outer diameter and 200 mm in height. Figure 2 displays the temperature–time curves during processing and phase diagram of the samples with different contents of Al. There are four stages during alloy processing. In stage I, the graphite tube was rapidly heated up to the temperature of ~300 K above the liquidus. In stage II, after the Si rocks were completely melted, the temperature was held for 30 min and the melt was stirred with a quartz rod every 5 min to ensure homogeneous mixing. Then, in stage III, the power of the furnace was reduced to lower the temperature of the melt to 50–100 K above the liquidus. The temperature gradient was measured by a K type thermocouple at the end of this stage, and the results are shown in Table 2. It should be noted that the temperature of 60%Al–Si alloy could not be measured because it is beyond the measuring range of the thermocouple. Finally, in stage IV, the alloy was solidified by pulling it out of the heater tube at a rate of 3 mm min^{-1}, which is approximately equal to the solidification rate. The samples were maintained under Ar atmosphere during the whole process.

Structure observation and composition measurement

The ingots were cut into two parts along their vertical axis. The cutting surface of one part was polished for structure observation. A plate 10 mm in thickness was cut with a saw from the other part and divided into 10 small bricks from the bottom to the top, as shown in Fig. 3.

The obtained bricks were weighed and put in a beaker with diluted hydrochloric acid to remove Al by their reaction, leaving primary silicon flakes and eutectic silicon powder. After the reaction was completed, the primary silicon flakes and the eutectic silicon powder were washed with deionised water, dried and weighed. Finally, mass fraction of Al of each brick can be calculated by

$$C_n = \frac{m_{total} - m_{Si} - m_S}{m_{total}} \quad (1)$$

where C_n, m_{total} and m_{Si} are the mass fraction of Al, total mass and Si mass of the nth brick from the bottom to the top of the plate. In addition, m_s is the mass of solid solution Si in Al matrix, which can be obtained from the Al–Si phase diagram.

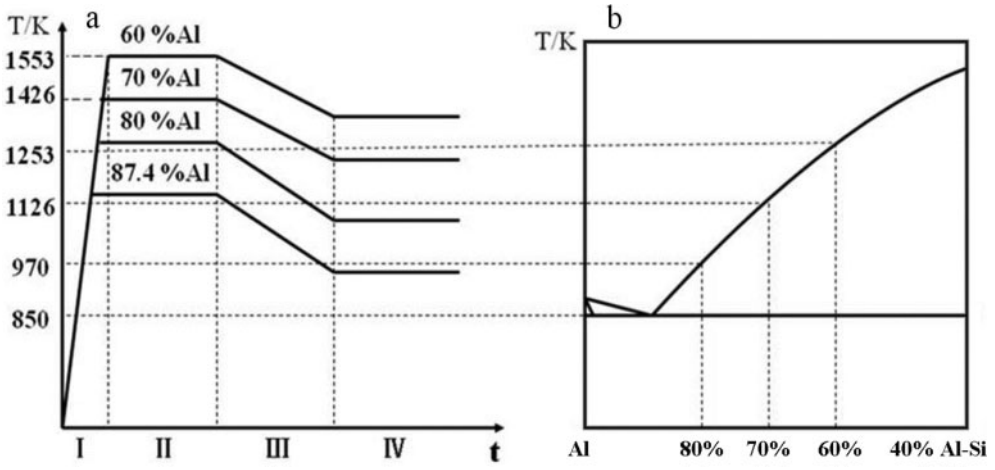

a temperature *T* versus time *t* curves during processing; *b* Al–Si phase diagram

2 Temperature–time curves of different samples

Table 2 Temperature gradient in melt

Composition/%Al	87.4	80	70
Top temperature/K	1070	1151	1275
Bottom temperature/K	950	1047	1193
Temperature gradient/K cm^{-1}	12	10.4	8.2

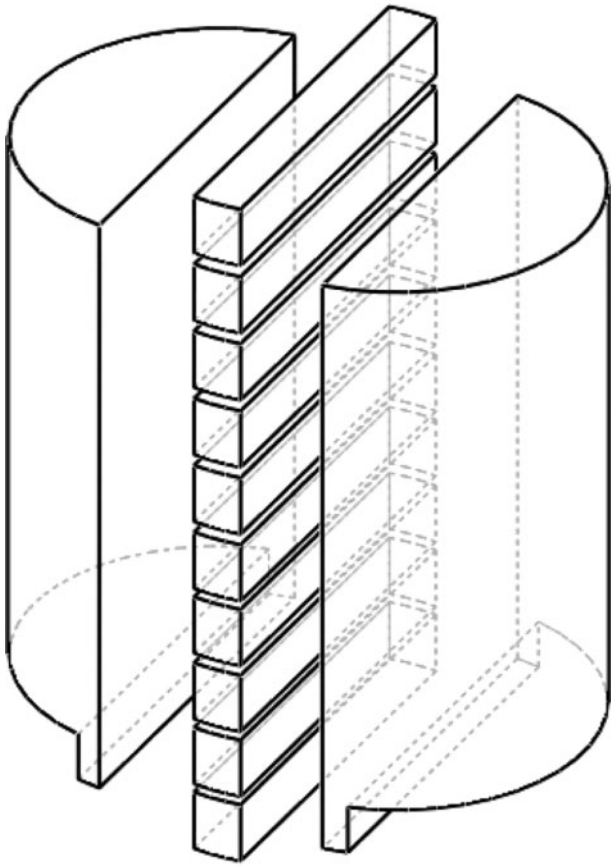

3 Sketch of cutting position of samples

Results and discussion

Macrostructure of solidified Al–Si ingots

Figure 4 shows the macrostructure of the solidified Al–Si ingots with different compositions. The diameter and height of the ingots are 80 and 125 mm respectively. It can be seen from this figure that the number of primary silicon plates decreases with increasing Al content. There are a large number of the primary silicon plates in 60%Al–Si alloy (Fig. 4*a*) and 70%Al–Si (Fig. 4*b*) alloy, mainly primary silicon grains in 80%Al–Si alloy (Fig. 4*c*), but no primary silicon in 87.4%Al–Si alloy (Fig. 4*d*). In the as presented three hypereutectic Al–Si alloy ingots (Fig. 4*a*–*c*), the quantity of the primary silicon plates decreases from the bottom to the top initially, then suddenly turns down to almost zero at a certain position and finally increases slowly in the top part of the ingots. In addition, tiny primary silicon plates can be seen near the bottom and the side surfaces of these ingots. All these facts indicate that the solidification of the hypereutectic Al–Si alloys is mainly directional except on the top of the ingot. In 87.4%Al–Si alloy (Fig. 4*d*), which is a eutectic alloy, directional solidification has no significant influence on the distribution of aluminium. The nucleation mechanism of the primary silicon phase at the top of the hypereutectic samples is that the impurity phases or oxides act as the nucleation sites, while the cooling argon gas, which was blown into the furnace continuously, provides the temperature gradient to drive it grow downward.

Moreover, it can be seen that there are two bulky eutectic areas in 80%Al–Si alloy, but such areas become smaller in 70%Al–Si alloy and even disappear in 60%Al–Si alloy. This can be explained by the melt flowing pattern during electromagnetic stirring as shown in Fig. 5. The viscosity of the Al–Si melt correlates with the temperature, as shown in equation (2)[16]

$$\mu(T) = \mu_0 \exp\left(\frac{E}{RT}\right) \tag{2}$$

where T is the absolute temperature, μ_0 a coefficient, E the activation energy and R the universal gas constant. When the temperature decreases, the viscosity of the Al–Si melt increases. Thus, the amount of convection and diffusion in the melt would be reduced. In the hypereutectic Al–Si alloys, the liquidus temperature drops when the Al content increases, so the amount of convection decreases with increasing Al content. As a result, in the hypereutectic Al–Si alloys, the higher the Al content, the harder the mixing of the melt.

Distribution of Al in Al–Si alloys

If there is enough time for solute diffusion to proceed to completion, the composition becomes uniform in both solid and liquid. This is equilibrium directional solidification, and three stages exist: initial transient immediately after the solidification starts, intermediate and the end of solidification.[17] In the hypereutectic Al–Si system, however, once the primary silicon phases are formed, they are hard to melt again during the solidification process. If the solute diffusion in the liquid is completed and the velocity of solidification is slow enough, the primary silicon grains could be formed at the bottom of the ingots and then grows up gradually.[18] Thus, the bottom with lower temperature is monolithic silicon phase, and the rest is a eutectic alloy.

However, in most cases during industrial production, the velocity of solidification is too fast to allow monolithic primary silicon grains grow at the bottom of the ingots. So, the above presented case is not applicable. As a matter of fact, at the beginning of solidification, the composition of the solid follows equilibrium solidification; as the solidification continues, the solute concentration ahead of the solid/liquid interface increases, forming a concentration gradient. In addition, the solute concentration of the solid phase will increase until the composition of liquid reaches the eutectic point. This process follows the Scheil relation

$$C_S = kC_0(1-x)^{k-1} \tag{3}$$

where C_s, k_0, C_0 and x are the solute content in the solid, segregation coefficient, the initial composition of the alloy and the mass fraction of the solid respectively. The assumption of Scheil model is that there is no diffusion in the solid and complete mixing in the liquid.

After the melt reaches the eutectic point, it remains at this composition until the end of solidification. The compositions from the bottom to the top of the ingots were measured and calculated through the method

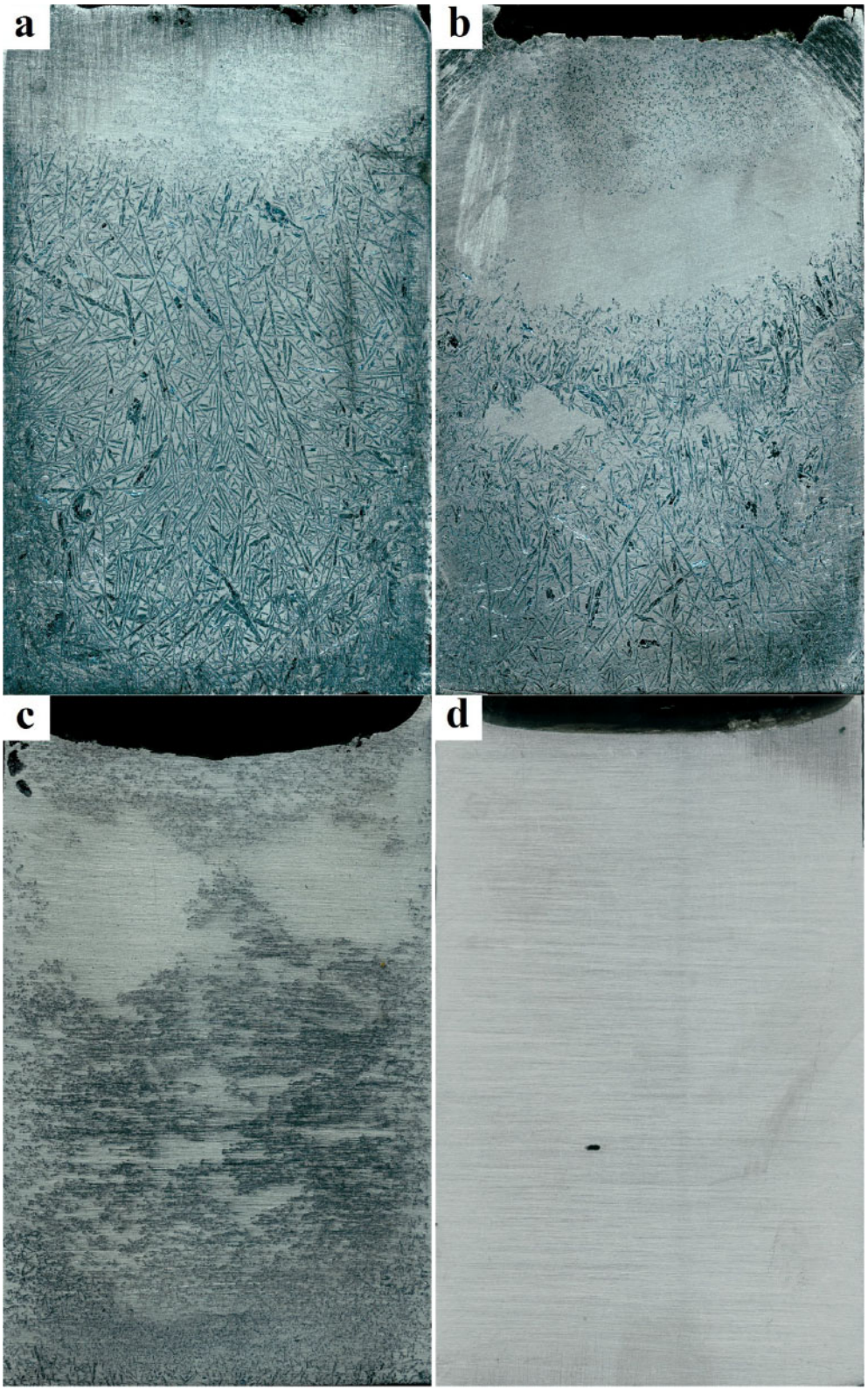

a 60%Al–Si; *b* 70%Al–Si; *c* 80%Al–Si; *d* 87.4%Al–Si

4 Macrostructure of solidified Al–Si ingots with different compositions

mentioned in the section on 'Structure observation and composition measurement'. The results are shown in Fig. 6. From the experimental data shown in Fig. 6, it can be seen that the distribution of Al in 60% and 70%Al–Si alloys agree with Scheil relation, which is mainly due to the higher temperature and lower convection in Al–Si melt as discussed in the section on 'Macrostructure of solidified Al–Si ingots'. So, equation (3) will be used to fit these two groups of data. The only unknown parameter k in the equation can be calculated by equation (4)

$$\int_0^a kC_0(1-x)^{k-1}dx = C_a\alpha \tag{4}$$

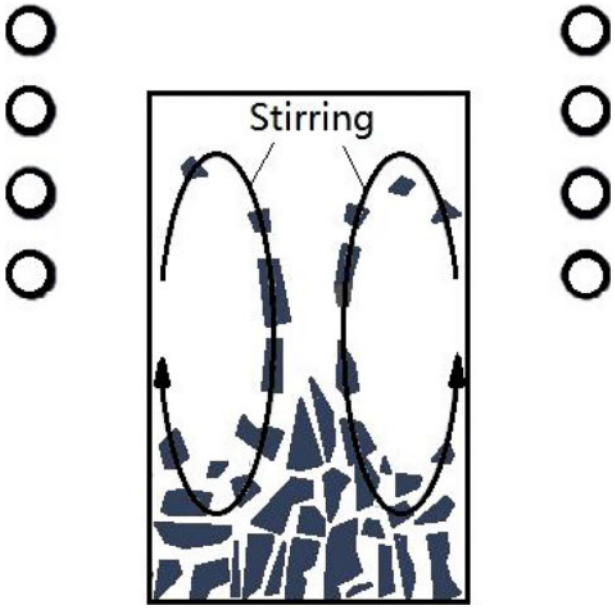

5 Schematic drawing of electromagnetic stirring mechanism

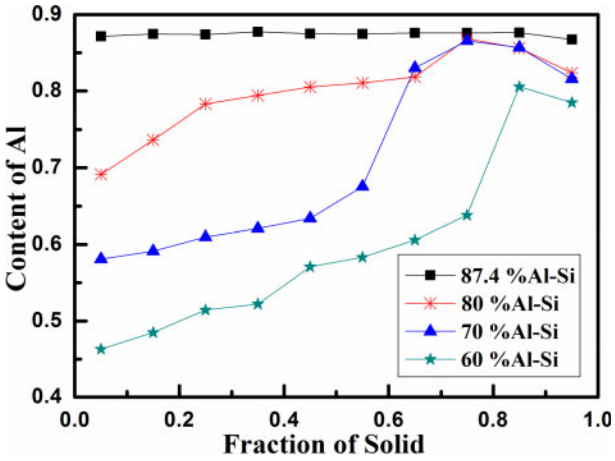

6 Measured contents of Al in samples with different initial compositions

Then,

$$k = \log_{1-a}\left(1 - \frac{C_a \alpha}{C_0}\right) \tag{5}$$

where a and C_a are the mass fractions of the solid phases at the point switching to the eutectic composition and the average composition of $0 \sim a$ respectively. C_a can be calculated from the experimental data. For 60%Al–Si alloy, $a = 0.75$, $C_0 = 0.6$, $C_a = 0.5478$ and thus $k = 0.8328$. For 70%Al–Si alloy, $a = 0.55$, $C_0 = 0.7$, $C_a = 0.6167$ and thus $k = 0.8299$.

The fitted C_s–x curves of these two alloys are illustrated in Fig. 7*a* and *b*. The curves consist of two parts: one is Scheil relation part ($0 \leqslant x \leqslant a$), and another is a eutectic composition line $C_s = 0.874$ ($a \leqslant x \leqslant 1$). It can be seen from these figures that the Scheil curves well reflect the data trend, but the last few points in these two figures are all below the eutectic composition line. There may be three factors that might have a contribution for this phenomenon. First, there are some primary silicon phases formed near the side surface of the ingots because of the lower temperature of the graphite support tube. Second, the impurities such as Fe, Ti, Ca and oxides are segregated to the top of the ingot. Third, because the top surface of the melt was cooled down by the applied argon gas filled into the furnace continuously, a few primary silicon phases might crystallise from the top surface into the melt. In addition, the third reason could explain why the data points trend downwards. Moreover, it can be seen from these two curves that the Scheil curve part as shown in Fig. 7*a* lasts longer than the one in Fig. 7*b*, indicating that it is easier to reach the eutectic point for the samples with higher Al content.

However, the distribution mechanism of Al in 80%Al–Si alloy is obviously different from those in the above two cases. So, the Scheil relation would not be applicable anymore. The liquidus temperature of the present alloy is only ~970 K, which is much lower than that of 60% and 70%Al–Si alloys. Moreover, because the induction heating power was reduced to reach the low melting temperature, the electromagnetic field intensity and stirring in the melt were reduced as well. As a result, mixing in this melt is very weak. Such alloy would just finish the initial transient stage during the directional solidification process. In addition, the solid reaches the initial composition C_0 and holds there until the composition of the melt is all eutectic. Finally, it solidifies as a eutectic alloy. Under this condition, the process of solute distribution follows the initial transient model as shown in equation (6). The assumption of the model is that there is no diffusion in solid and limited diffusion in liquid.

$$C_S = C_0 = \left[1 - (1 - k)\exp\left(-k\frac{V}{D}x\right)\right] \tag{6}$$

where V and D stand for the velocity of solidification and diffusion coefficient respectively. Although these two parameters are unknown in the experiment, they are all fixed values in this case. So, if rewrite $R = V/D$, then on integration equation (6) becomes

$$\int_0^a C_0[1 - (1 - k)\exp(-kRx)]dx = C_a\alpha \tag{7}$$

Then,

$$C_0\exp(-akR)[1 - k + \exp(akR)(-1 + k + akR)] = akRC_a \tag{8}$$

which is an implicit function about k and R, where $C_0 = 0.8$, $a = 0.65$ and $C_a = 0.7769$.

A C_s–x curve for the experimental solute distribution in 80%Al–Si alloy was fitted by least square method. First, in the 60% and 70%Al–Si alloys, the value of the apparent segregation coefficient k was set at ~0.8, and R can be calculated by equation (8). By iterative method, the corresponding k and R of the present alloy were determined to be 0.821 and 9.8 respectively. Finally, the C_s–x curve can be drawn by equation (6) with the values of k and R inserted. In addition, the fitted C_s–x curve of the alloy is illustrated in Fig. 7*c*.

For 87.4%Al–Si alloy, the initial composition C_0 is eutectic, so the composition of the ingot solid can reach the eutectic point at the beginning of the solidification. In other words, it may be regarded as $k = 1$ in equation (6). Figure 7*d* presents the C_s–x line of the alloy. From this figure, it can be seen that only the last point is obviously

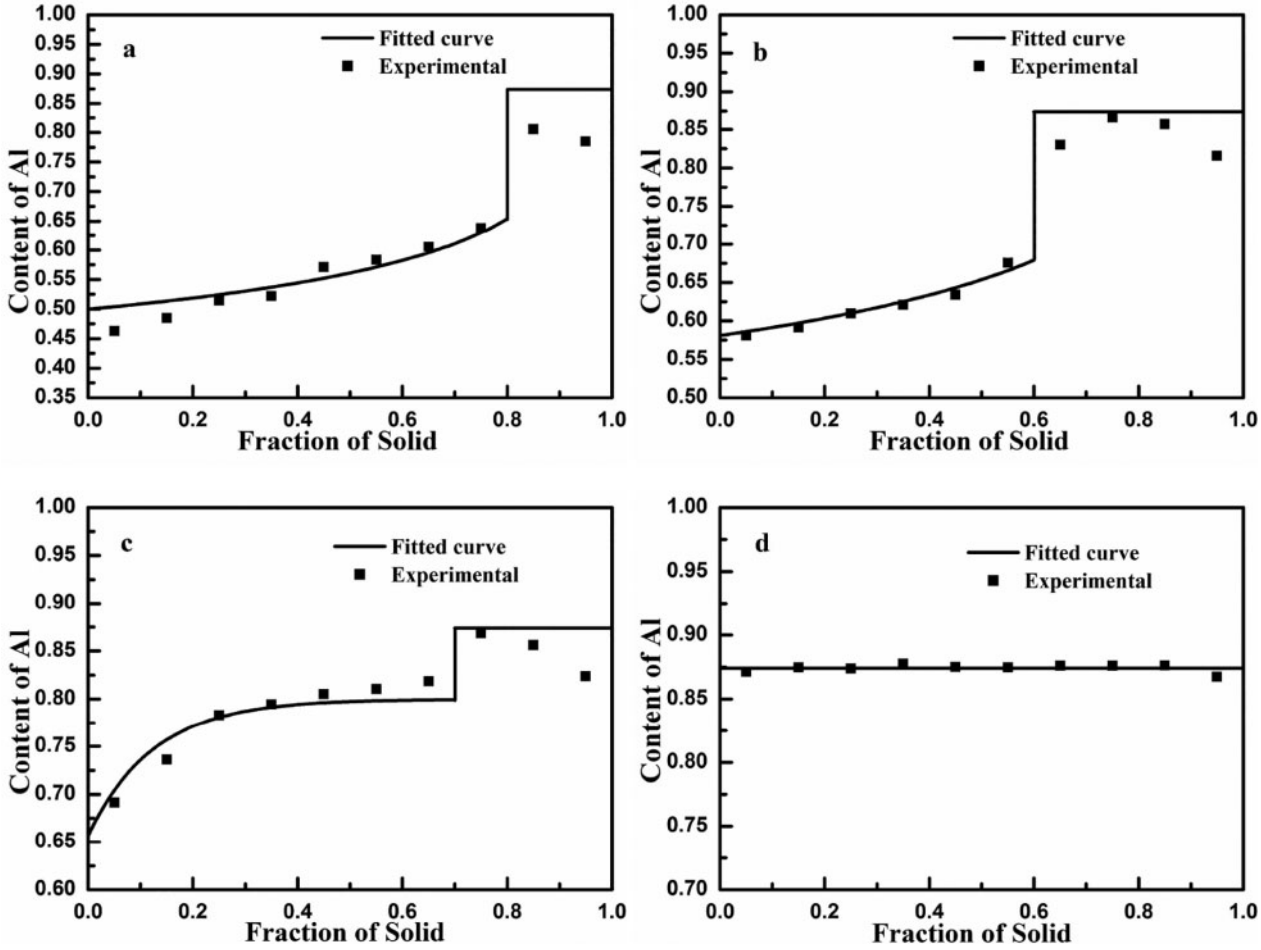

a 60%Al–Si; *b* 70%Al–Si; *c* 80%Al–Si; *d* 87.4%Al–Si

7 Fitted Al distribution of obtained Al–Si alloys

below the fitted line, which might be caused by the metal impurities and oxides segregated there.

It should be noted that, from the above fitted curves, the apparent segregation coefficient k was calculated at ~0.83 for the hypereutectic Al–Si alloys in this work. However, the equilibrium segregation coefficient of Al in the Al–Si system is only 0.0028, which is much smaller than the apparent one. There are three factors responsible for the phenomenon. First, the process of solidification in this work is non-equilibrium. The velocity of the solidification is much faster than that required by equilibrium solidification, so the solute could not diffuse and be mixed completely at the solid/liquid interface. Second, the equilibrium segregation coefficient was calculated under a hypothesis that the liquidus and the solidus lines in the Al–Si phase diagram are all straight lines, which is adaptable only in the case of pure silicon with a little of Al. Finally, the temperature gradient at the solid/liquid interface might not be set perfectly to keep the interface flat. As a result, the equilibrium segregation coefficient could not describe the solute distribution during non-equilibrium solidification. On the contrary, the apparent segregation coefficient proposed in this work fits the situation well.

Conclusions

It was found that during the EMCC process, there are two types of aluminium distribution patterns in the hypereutectic Al–Si alloys: Scheil model for 60% and 70%Al–Si alloys with higher solidification temperature and the initial transient model for 80%Al–Si alloy with lower solidification temperature. An apparent segregation coefficient of Al is proposed to characterise the solidification process, which is ~0.83 for the hypereutectic alloys. However, Al distributes evenly in the eutectic Al–Si alloy.

Acknowledgements

This work was financially supported by the National Natural Science Foundation of China (nos. 51404231 and 51474201); "100-talent Program" of Chinese Academy of Sciences, Anhui Provincial Natural Science Foundation (no. 1508085QE81) and Science Fund of Institute of Plasma Physics, Chinese Academy of Sciences (grant nos. 095YZ31222 and Y35QT10894).

References

1. Q. L. Li, T. D. Xia, Y. F. Lan and P. F. Li: 'Effects of melt superheat treatment on microstructure and wear behaviours of hypereutectic Al-20Si alloy', *Mater. Sci. Technol.*, 2014, **30**, 835–841.
2. Q. Luo, Q. Li, J. Y. Zhang, S. L. Chen and K. C. Chou: 'Experimental investigation and thermodynamic calculation of the Al-Si-Ti system in Al-rich corner', *J. Alloys Compd*, 2014, **602**, 58–65.
3. H. Drar and I. L. Svensson: 'Improvement of tensile properties of Al-Si alloys through directional solidification', *Mater. Lett.*, 2007, **61**, 392–396.

4. H. Drar and I. L. Svensson: 'Characterization of tensile properties and microstructures in directionally solidified Al-Si alloys using linear roughness index', *Mater. Charact.*, 2006, **57**, 244–258.
5. D. Sollmann: '6N pure and simple', *Photon Int.*, 2009, 110–113.
6. T. Yoshikawa and K. Morita: 'Removal of phosphorus by the solidification refining with Si-Al melts', *Sci. Technol. Adv. Mater.*, 2003, **4**, 531–537.
7. L. Hu, Z. Wang, X. Gong, Z. Guo and H. Zhang: 'Impurities removal from metallurgical-grade silicon by combined Sn-Si and Al-Si refining processes', *Metall. Mater. Trans. B, 44B*, 2013, 828–836.
8. J. W. Li and Z. C. Guo: 'Thermodynamic evaluation of segregation behaviors of metallic impurities in metallurgical grade silicon during Al-Si solvent refining process', *J. Cryst. Growth*, 2014, **394**, 18–23.
9. J. C. Jie, Q. C. Zou, J. L. Sun, Y. P. Lu, T. M. Wang and T. J. Li: 'Separation mechanism of the primary Si phase from thehypereutectic Al-Si alloy using a rotating magnetic field duringsolidification', *Acta Mater.*, 2014, **72**, 57–66.
10. T. Yoshikawa and K. Morita: *Refining of silicon by the solidification of Si-Al melt with electromagnetic force, ISIJ Int.*, 2005, **45**, 967–971.
11. T. Yoshikawa and K. Morita: 'Removal of B from Si by solidification refining with Si-Al melts', *Metall. Mater. Trans. B, 36B*, 2005, 731–736.
12. T. Yoshikawa and K. Morita: 'Refining of silicon during its solidification from a Si-Al melt', *J. Cryst. Growth*, 2009, **311**, 776–779.
13. W. Yu, W. Ma, G. Lü, Y. Ren, H. Xue and Y. Dai: 'Si purification by enrichment of primary Si in Al-Si melt', *Trans. Nonferrous Met. Soc. China*, 2013, **23**, 3476–3481.
14. S. P. Nikanorov, L. I. Derkachenko, B. K. Kardashev, B. N. Korchunov, V. N. Osipov and V. V. Shpeizman: 'Structural and physicomechanical properties of directionally crystallized aluminum-silicon alloys', *Phys. Solid State*, 2013, **55**, 1207–1213.
15. M. D. Peres, C. A. Siqueira and A. Garcia: 'Macrostructural and microstructural development in Al-Si alloys directionally solidified under unsteady-state conditions', *J. Alloys Compd*, 2004, **381**, 168–181.
16. L. Battezzati and A. L. Greer: 'The viscosity of liquid metals and alloys', *Acta Metall.*, 1989, **37**, 1791–1802.
17. D. M. Stefanescu: 'Science and engineering of casting solidification', 2nd edn, 36, ; 2008, Columbus, OH, Springer.
18. Y. Nishi, Y. Kang and K. Morita: 'Control of Si crystal growth during solidification of Si-Al melt', *Mater. Trans.*, 2010, **51**, 1227–1230.